

Optimized magnetic resonance diffusion protocol for ex-vivo whole human brain imaging with a clinical scanner

Benoit Scherrer^a, Onur Afacan^a, Aymeric Stamm^a, Jolene Singh^a and Simon K. Warfield^a

^aBoston Children’s Hospital, Department of Radiology
300 Longwood Avenue, Boston, MA, 02115, USA

ABSTRACT

Diffusion-weighted magnetic resonance imaging (DW-MRI) provides a novel insight into the brain to facilitate our understanding of the brain connectivity and microstructure. While *in-vivo* DW-MRI enables imaging of living patients and longitudinal studies of brain changes, post-mortem *ex-vivo* DW-MRI has numerous advantages. *Ex-vivo* imaging benefits from greater resolution and sensitivity due to the lack of imaging time constraints; the use of tighter fitting coils; and the lack of movement artifacts. This allows characterization of normal and abnormal tissues with unprecedented resolution and sensitivity, facilitating our ability to investigate anatomical structures that are inaccessible *in-vivo*. This also offers the opportunity to develop today novel imaging biomarkers that will, with tomorrow’s MR technology, enable improved *in-vivo* assessment of the risk of disease in an individual. Post-mortem studies, however, generally rely on the fixation of specimen to inhibit tissue decay which starts as soon as tissue is deprived from its blood supply. Unfortunately, fixation of tissues substantially alters tissue diffusivity profiles. In addition, *ex-vivo* DW-MRI requires particular care when packaging the specimen because the presence of microscopic air bubbles gives rise to geometric and intensity image distortion. In this work, we considered the specific requirements of post-mortem imaging and designed an optimized protocol for *ex-vivo* whole brain DW-MRI using a human clinical 3T scanner. Human clinical 3T scanners are available to a large number of researchers and, unlike most animal scanners, have a bore diameter large enough to image a whole human brain. Our optimized protocol will facilitate widespread *ex-vivo* investigations of large specimen.

Keywords: Diffusion-weighted magnetic resonance imaging, Protocol, Ex-vivo, Human clinical scanner, Diffusion compartment imaging

(draft version)

1. INTRODUCTION

Diffusion-weighted magnetic resonance imaging (DW-MRI) provides a novel insight into the brain to facilitate better understanding of the brain connectivity and microstructure in healthy anatomy and in disease. *In-vivo* and *ex-vivo* DW imaging both have their advantages. *In-vivo* DW-MRI enables non-invasive imaging of living patients and longitudinal analysis of structural changes in clinical practice and in research. In contrast, post-mortem *ex-vivo* imaging provides greater spatial resolution due to the lack of imaging time constraints. It enables unlimited scanning time without movement artifact and offers the opportunity to use tighter fitting coils, providing higher SNR.¹ This creates the opportunity of characterizing normal and abnormal tissues with unprecedented spatial resolution and sensitivity, providing insight into small anatomical structures that are inaccessible *in-vivo*. In the aggregate, *ex-vivo* imaging holds promise for facilitating better understanding of the healthy brain anatomy and enables the development of novel imaging biomarkers that will, with tomorrow’s MR technology, provide improved *in-vivo* assessment of the risk of disease in an individual.

Post-mortem studies, however, generally rely on the fixation of specimen to inhibit tissue decay which starts as soon as tissue is deprived from its blood supply. Unfortunately, fixation of tissues substantially alters tissue diffusivity profiles.² In addition, *ex-vivo* DW-MRI requires particular care when packaging the specimen because

Further author information: (Send correspondence to Benoit Scherrer)
Benoit Scherrer: E-mail: benoit.scherrer@childrens.harvard.edu

the presence of microscopic air bubbles substantially impacts the echo planar imaging (EPI) slice read-out trajectory used in DW-MRI, giving rise to images with geometric and intensity distortion.

Importantly, the choice of parameters of a DW-MRI protocol strongly depends on the diffusion model considered for analysis. The DW-MRI model used most often is diffusion tensor imaging (DTI),³ which describes the average diffusion direction and strength at each voxel at a single diffusion scale with a diffusion tensor. Characterization of the diffusion with DTI has been shown to be sensitive to detecting abnormal tissues, e.g., as in traumatic brain injury,⁴ in schizophrenia⁵ and in neurodegenerative disease.⁶ DTI, however, only provides a macroscopic summary of the diffusion in each voxel. It describes the diffusion in each voxel with a model with only 6 degrees of freedom and is unable to 1) capture the intra-voxel orientation heterogeneity (IVOH) of WM fascicle in voxels; and 2) separately characterize the spectrum of isotropic diffusion components arising from the presence of partial voluming with cerebro-spinal fluid (CSF)⁷ and of neuroinflammation and edema.⁸ Therefore, while DTI is, to some extent, sensitive to detecting microstructural changes in disease, it shows poor specificity in depicting the precise nature of these changes.^{9,10}

Many models have been proposed to overcome DTI's limitations, including constrained spherical deconvolution (CSD)¹¹ and q-ball imaging (QBI).¹² CSD and QBI rely on an acquisition with a single non-zero b-value and primarily seek to characterize the orientation profile of the diffusion in order to assess the connectivity. However, they do not model the signal decay as a function of b-value. The information about various diffusion scales is missed and the ability to describe the underlying microstructure is limited.

Instead, a primary alternative is diffusion compartment imaging (DCI), which reflects the presence of tissue compartments within voxels¹³ (e.g., partial voluming with CSF and with multiple white matter fascicles within a voxel¹⁴) and relates biophysical features of each compartment to the measured DW signal with a generative model. Estimation of the DCI model parameters from the acquired DW images corresponds to solving an inverse problem and enables extraction of structural information at a sub-voxel resolution.^{13,15,16} Importantly, DCI allows for the characterization of each fascicle in each voxel. It provides insight into both neural connectivity and microstructural tissue changes with improved sensitivity and specificity compared to DTI.¹⁷ However, DCI requires the acquisition of multiple non-zero b-values to distinguish between the decay curves of each compartment in each voxel.^{14,18,19}

In this work, we considered the specific requirements of post-mortem imaging and, building upon previous *ex-vivo* protocols proposed in the literature,^{20,21} designed an optimized, multiple b-value protocol for *ex-vivo* whole brain DCI using a human clinical 3T scanner. Human clinical 3T scanners are available to a large number of researchers and, unlike most animal scanners, have a bore diameter large enough to image a whole human brain. Our protocol will facilitate widespread DCI *ex-vivo* investigations of large specimen in research.

The paper is organized as follows. In Section 2, we detail each step of our protocol including the choice of imaging solvent, of specimen container, of field-of-view placement and of projective and retrospective distortion correction strategy. We also describe the choice of diffusion gradient table and b-value range to enable diffusion compartment imaging. We report results in Section 3 and conclude in Section 4.

2. MATERIAL AND METHODS

Brain fixation. Fixation is necessary to inhibit tissue decay, or autolysis, which starts as soon as tissue is deprived of its blood supply. As commonly used in the literature,^{20,21} we immersed the specimen in 10% neutral-buffered Formalin (4% formaldehyde) to inhibit the autolysis of tissues and to preserve tissues and cellular morphology.

Choice of a solvent during imaging. Imaging a specimen for multiple hours requires the use of a solvent to prevent the tissues from drying and deteriorating. Some studies have imaged brains in fixative solution such as Formalin.²⁰ However, and consistently with Miller *et al.*,²¹ we found that this solvent gave rise to a very large background signal due to its high proton content, limiting the dynamic range of the tissue intensities

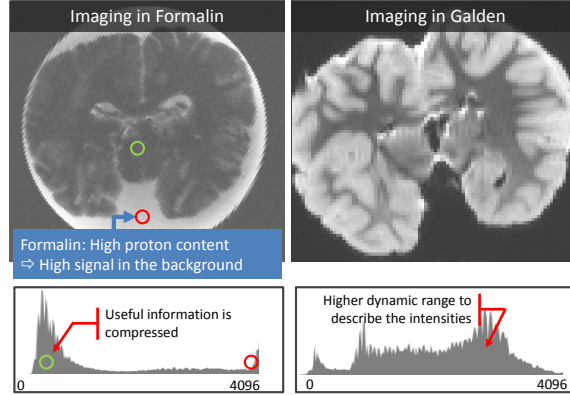


Figure 1. Illustration of the limited dynamic range when a solvent with high proton content is used. A high proton content solvent such as Formalin gives rise to a large background signal intensity ($i_{\text{background}}$) compared to the intensity of tissues (i_{tissues}) ($i_{\text{background}} \gg i_{\text{tissues}}$). Because the numerical encoding of intensities is limited with MRI scanners (e.g., each intensity is encoded with a 12 bits integer number on Siemens scanners), a high maximum intensity in the background reduces the ability to encode lower intensities corresponding to tissue (left). In contrast, using a proton-free solvent enables description of the tissue intensity with all the available range of intensity values (right).

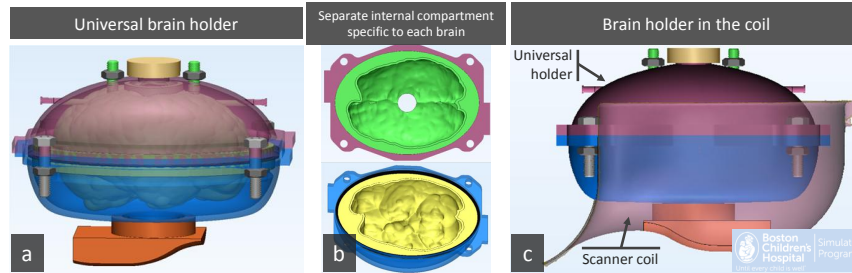


Figure 2. Design of the 3-D printed brain holder. Illustration of the universal holder base (orange, blue and pink parts in Fig.a) and of the top and bottom separate compartments specific for a brain (green and yellow parts in Fig.b). Fig.c shows a 3-D rendering of the brain holder sitting in the scanner coil.

(See Fig. 1a). We instead used Galden which does not contain protons and therefore does not give rise to MR signal in the background. In addition, Galden is a highly viscous oil which has the additional advantage of limiting potential brain motion that may be caused by the application of diffusion-sensitizing gradients in DW-MRI.

Specimen container. We investigated two containers for imaging specimen:

- *3-D printed brain holder.* A 3-D printed brain holder was designed to support the brain and to minimize brain motion. First, a universal holder base was designed and printed with hard transparent plastic to fit exactly in our scanner coil (orange, blue and pink parts in Fig. 2a/b). Second, internal compartments specific for each brain were designed (yellow and green parts in Fig. 2a) to fit in the universal holder base. The brain-specific compartments were obtained by acquiring a CT image of the brain from which the cortical surface was extracted. The image was smoothed with Gaussian filtering and then dilated by 5mm to define the brain holder walls. The brain-specific compartments were printed with transparent plastic too. The strategy of using a separated universal base and internal compartments for each brain was chosen to reduce printing plastic consumption in the long term.
- *Brain bagging.* We also considered packing the brain specimen into a sealed, close-fitting bag to minimize the distance between the loop coil and the sample. A shaker was used to ensure even distribution of fluid. Since water-based solutions such as Formalin are less dense than Galden, any remnants of the fixative solution floated to the top and could be easily discarded. Because brain tissue is less dense than Galden, it was useful to partially seal the tissue in the bag before pouring in the Galden. Adding a few angled seals

at the top of the bag allowed air bubbles to be vacuumed out, and allowed more space for Galden to be delivered. Once the sample was fully immersed in the Galden, a final seal was placed in the bag. The seal was inspected all around before imaging.

Prospective minimization of DW image distortion by elimination of air bubbles. Conventional DW-MRI sequences employ echo planar imaging (EPI) read-out to rapidly acquire each slice after the RF slice excitation. EPI, however, is very sensitive to magnetic field inhomogeneities caused by susceptibility changes at tissue interface such as air and tissue interface. The field inhomogeneity gives rise to phase perturbation in k-space which accumulates during the acquisition of each slice.²² This results in severe distortion in the form of voxel shifts in the image space, of largest magnitude along the phase-encoding direction.²³ The accumulation of phase perturbation (and therefore the amount of distortion) is especially large when high spatial resolution EPI is sought because of the large number of phase-encodes employed. This makes high resolution ex-vivo DW-MRI imaging very sensitive to the presence of microscopic air bubbles in tissue samples.

To minimize the presence of air bubbles, we required an overnight-24 hr immersion of the brain in a bucket of Galden prior to transferring the brain to the custom-made holder or to the brain bag. Then, we kept the brain in its container (3-D printer holder or bag) for a second 24h prior imaging, regularly and slowly rotating the container to facilitate the extraction of air bubbles. Full immersion with rotation allowed air bubbles to escape from the ventricles. The brain holder could easily be refilled with more Galden to replace the volume freed by air bubbles. Additional angled seals at the top of the brain bag were applied to isolate air bubbles when the brain bag strategy was used.

Scanner and coil setup. The acquisitions were achieved on a 3T Siemens Skyra scanner with a 64 channel head coil and a 7mm loop coil. The 3-D printed brain holder was designed to fit inside a 64 channel head coil such that the specimen is at similar distance to the anterior and posterior elements of the coil. With this setup all 64 coils were utilized, but the distance from the coils to the specimen was higher compared to the plastic bag. With the plastic bag, the tissue was close to the posterior element of the tissue but much farther to the anterior element. Therefore we used a 7mm surface coil instead of the anterior element.

Choice of image acquisition orientation during MR scanning. The orientation of the MR acquisition was chosen to obtain the smallest possible field of view to minimize the matrix size at the desired spatial resolution. This enabled reduction of the number of phase encodes for each slice and therefore reduced the amount of image distortion caused by the susceptibility artifact. We found that the coronal acquisition orientation with phase encoding direction set as HF or FH offered the smallest number of phase encodes at the desired isotropic spatial resolution.

Quantitative T2 mapping. In order to optimize the imaging parameters for diffusion acquisition, T2 relaxation time of the tissue was measured. This was achieved by acquiring a multi-slice spin echo sequence with 5 echoes (echoes: 13, 26, 39, 52, 65ms; in-plane resolution: 0.5mm; slice thickness: 3mm) and by fitting an exponential T2 decay curve with stimulated echo correction using Levenberg Marquardt algorithm.

While T2 is typically on the order of 80ms at 3T in the adult brain white matter *in-vivo*,²⁴ T2 can be much higher in early brain development (up to 150-300ms)²⁵ and is substantially reduced by fixation.²⁶ Measuring the T2 is important because it provides insight into the expected quality of diffusion weighted images. Indeed, the measured attenuated DW signal S exponentially decreases with decreasing T2, as described by the relation:

$$S = S_0 \exp\left(-\frac{TE}{T_2}\right) \exp(-bD), \quad (1)$$

where S_0 is the $b = 0\text{s/mm}^2$ signal with no gradient gradient applied, TE is the echo time, b is the b-value and D is the apparent diffusion coefficient (ADC). Assessment of the T2 in post-mortem tissues provides insight into the expected DW signal amplitude (see Fig. 3) and therefore into the expected signal-to-noise ratio (SNR) of DW images. This may guide the choice of number of repetitions needed to obtain DW images with a desired SNR.

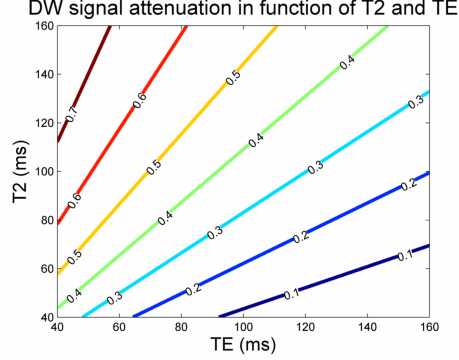


Figure 3. Plot of the isolines of $\exp(-\frac{TE}{T2})$ for varying TE and T2 representing the multiplicative DW signal attenuation due to TE and T2. It shows that those two parameters have a substantial impact on the signal amplitude and therefore on the SNR of DW images, regardless of the b-value applied.

Gradient encoding set. Characterization of both the connectivity and of microstructural properties with diffusion compartment imaging (DCI) requires the acquisition of multiple non-zero b-values to disentangle the signal arising from each compartment in each voxel.^{14, 18, 19} Varying the b-value in a pulse gradient spin echo (PGSE) DW-MRI sequence can be achieved by either modification of the diffusion pulse gradient duration δ , the separation time Δ between the pulses or the norm of the applied diffusion sensitization gradient $\|\mathbf{g}\|$, as described by Le Bihan:²⁷

$$b = \gamma^2 \delta^2 (\Delta - \delta/3) G^2 \|\mathbf{g}\|^2, \quad (2)$$

where γ the gyromagnetic ratio and G is the scanner maximum gradient strength.

Imaging multiple b-values is often achieved by using a multiple shell HARDI. Unfortunately, imaging large b-values with a multiple shell HARDI requires an acquisition with extended echo time (TE). This is especially true when using a clinical scanner, for which the maximum gradient strength G is limited and high b-values are obtained by using long duration δ and Δ and therefore long TE. The long duration TE leads, in turn, to an exponentially lower SNR for all the b-value shells due to T2 relaxation (see Eq. (1) and Fig. 3). Equal SNR might be achieved by repeating the measurements but leads to significantly increased scan times.

Instead, we employed the CUSP (Cube and Sphere) gradient set¹⁴ which combines spherical and cubic sampling in q -space (see Fig. 4). CUSP is based on the modification of a 2-shell HARDI. In contrast to a multi-shell HARDI, the pulse duration and separation δ and Δ of the PGSE sequence are fixed to achieve the b-value of the inner shell (instead of the outer-shell for multi-shell HARDI), which requires a shorter TE and provides a significant SNR boost. The gradients of the outer shell have maximally separated gradients orientation with respect to the inner shell²⁸ but cannot be imaged with the fixed low δ and Δ . Instead, we reduce their strength (red gradients) so that they lie in the cube enclosing the inner shell. This cube is a cube of constant TE in q -space, in which any gradient can be imaged without modification of δ and Δ but by modification of $\|\mathbf{g}\|$. This enables imaging b-values up to three times the b-value of the inner-shell, corresponding to the diffusion gradients $\mathbf{g} = (\pm 1, \pm 1, \pm 1)$, with low TE defined by the inner-shell. Using a gradient $\mathbf{g} = (\pm 1, \pm 1, \pm 1)$ corresponds to imaging high b-values by using maximum current intensity in all the diffusion gradient encoding coils simultaneously, without increasing TE.

We designed a CUSP gradient set in which high-norm vectors (*i.e.*, high b-value images) are preceded by a $b = 0 \text{ s/mm}^2$ and distributed through the entire scan to reduce the scanner burden (see Appendix). For a given largest imaged b-value, the TE gain of CUSP compared to a multiple-shell HARDI was on the order of 30ms to 40ms at 3 Tesla with $G = 40 \text{ mT/m}$, which is equivalent to a *two- to three-fold* reduction in scan time at equal SNR.

Choice of the optimal b-value range. Scherrer *et al.*¹⁴ suggested that the b-value of the inner shell of CUSP should be set to the optimal b-value b_{optimal} for imaging the white matter. This allows imaging of a spherical sampling at $b=b_{\text{optimal}}$ with uniformly distributed gradient orientations as well as other additional

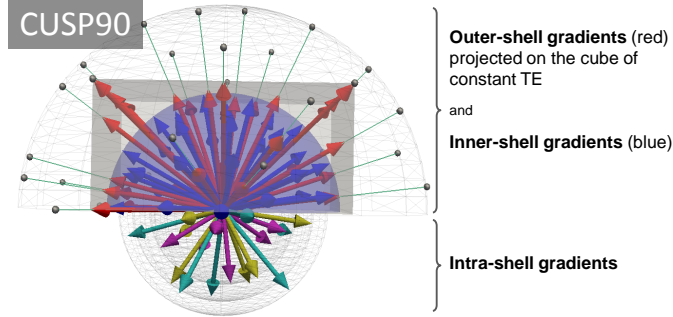


Figure 4. The CUSP90 gradient encoding scheme. Intra-shell gradients are shown in a different hemisphere than inner-shell and outer-shell gradients for visualization purpose.

b-value images up to $3b_{\text{optimal}}$ with low TE and therefore high SNR. Jones *et al.*²⁹ showed that, when estimating an apparent diffusion coefficient ADC from two measurements, the optimal non-zero b-value that minimizes the estimation error was given by $b_{\text{optimal}} = 1.11/\text{ADC}$. This typically leads to $b_{\text{optimal}} \approx 1000\text{s}/\text{mm}^2$ in the *in-vivo* adult brain white matter.

Preliminary *ex-vivo* DW-MRI acquisitions at our institution identified ADC values in the order of $1.8\text{E}^{-4}\text{mm}^2/\text{s}$ to $3.6\text{E}^{-4}\text{mm}^2/\text{s}$ in fixed specimens, leading to b_{optimal} between $3000\text{s}/\text{mm}^2$ and $6000\text{s}/\text{mm}^2$ according to Jones *et al.*²⁹ However, imaging the inner shell of CUSP with such a high b-value is challenging with a clinical scanner because clinical scanners have a relatively limited maximum gradient strength (typically $20\text{mT}/\text{m}$ to $70\text{mT}/\text{m}$ compared to several hundreds of mT/m on animal scanners). As a consequence, high b-values for unit-norm gradients are imaged by using long gradient pulse duration δ and separation Δ (see Eq. (2)). This leads, in turn, to long duration TE and therefore exponentially attenuated signal and low SNR for all the images due to T2 relaxation, regardless of the applied b-value (See Eq. (1)).

This highlights a fundamental trade-off in *ex-vivo* DW-MRI imaging with a clinical scanner: while high b-values $3000 - 6000\text{s}/\text{mm}^2$ may in theory minimize the error in model parameters,²⁹ imaging high b-values also leads to a substantial SNR loss due to increased TE (in addition to lower SNR due to increased diffusion sensitization) that may counter-balance the benefit of using high b-values.

We evaluated this trade-off by comparing at each voxel confidence intervals on the estimated ADC when using a single-shell HARDI with $b = 1000\text{s}/\text{mm}^2$ (minimum achievable TE: 95ms) and a single-shell HARDI with $b = 2000\text{s}/\text{mm}^2$ (minimum achievable TE: 107ms). Confidence intervals were computed by using *residual bootstrapping*³⁰ and by assessing the variance of ADC across model estimated at each bootstrap iteration. Contrary to the wild bootstrap,³¹ the residual bootstrap does not assume any symmetry in the distribution of the residuals, which has been shown to lead to smaller biases and reduced overall errors, leading ultimately to more accurate estimates of confidence intervals.³⁰

Correction of residual geometric and intensity distortions. While the presence of air bubbles was minimized prior scanning, residual microscopic air bubbles may remain and give rise to residual geometric and intensity distortion. We acquired each CUSP scans twice using opposite phase encoding directions between each scan (HF and FH). This resulted, for each diffusion gradient orientation, in pairs of DW images with opposite geometric distortions caused by the susceptibility artifact. The susceptibility-induced off-resonance field was estimated from the pairs of $b = 0\text{s}/\text{mm}^2$ images using Topup implemented in FSL.³² All the DW images were then corrected using the estimated off-resonance field.

Acquiring all the diffusion gradient orientations with opposite phase encoding direction provides improved intensity distortion correction compared to acquiring only the $b = 0\text{s}/\text{mm}^2$ images with opposite phase encoding direction. Indeed, correcting for intensity distortion in regions of local geometric compression (*i.e.*, regions in which the signals from different voxels 'pile up' in a voxel) corresponds to a 'one-to-many' ill-posed correspondence problem. Imaging these regions using opposite phase encoding direction leads to regions of local geometric expansion (see Fig. 7) (many-to-one correspondence problem) which enables image intensity correction.

Diffusion Compartment Imaging with $1 \times 1 \times 1\text{mm}^3$ isotropic spatial resolution. We imaged a one-month old newborn ex-vivo brain. Acquisitions were approved by the Institutional Review Board (IRB). We considered a CUSP gradient table with 90 gradient orientations (see Fig. 4 and Appendix) containing a large number of different b-values:

- 12 images with $b = 0\text{s/mm}^2$
- 30 gradients on the inner shell at $b = b_{\text{inner}}$
- 30 gradients on the cube of constant TE providing gradients with b-values between $b_{\text{inner}} < b \leq 3b_{\text{inner}}$
- 3 intra-shells of 6 directions each at $0.4b_{\text{inner}}$, $0.6b_{\text{inner}}$ and $0.8b_{\text{inner}}$

Based on preliminary scans to determine the optimal b-value range (see Section 3) we used $b_{\text{inner}} = 1000\text{s/mm}^2$. The echo time using this CUSP90 was only 95ms, while b-values up to 3000s/mm^2 corresponding to gradient vectors $g = (\pm 1, \pm 1, \pm 1)$ were acquired. Other parameters were: matrix size = 128×76 , FOV= $128\text{mm} \times 76\text{mm}$, resolution= $1 \times 1 \times 1\text{mm}^3$, coronal orientation, 60 slices. Parallel imaging with an acceleration factor of 2 was used to reduce the number of phase encoding line to 54. The scan time duration for one CUSP90 was 17 minutes. A total of 17 repetitions with phase encoding HF and 17 repetitions with phase encoding FH was acquired. After each repetition, a 6 minute pause was added to reduce the load on the gradients, leading to a total scan duration time of 13h02min. We also acquired a T2-weighted turbo spin echo (TSE) with spatial resolution $0.45 \times 0.45 \times 2\text{mm}^3$ for visualization purpose.

We considered a DCI model that reflects the presence of tissue compartments in each voxel and captures the non-monoexponential decay of the diffusion observed in voxels. More precisely, we considered that each compartment is in slow exchange and modeled the signal arising from each of them with a diffusion tensor. We considered in each voxel a multi-tensor model (MTM)^{14,33} with 1) an isotropic diffusion compartment to model the diffusion of free water; and 2) a series of anisotropic diffusion compartments to model the combined contribution of hindered and intra-axonal diffusion arising from each WM fascicle, leading to the attenuation DW signal $S_i(\mathbf{g}_g, b_g)$:

$$S_i(\mathbf{g}_g, b_g) = S_0 \left[f_{0,i} \exp(-D_{\text{iso}} b_g) + \sum_{j=1}^{N_i^f} f_{j,i} \exp(-b_g \mathbf{g}_g^T \mathbf{D}_{j,i} \mathbf{g}_g) \right], \quad (3)$$

where \mathbf{g}_g is a unit-norm diffusion gradient, b_g the corresponding b-value, N_i^f is the number of WM fascicles at voxel i , $\{f_{j,i}, j = 1, \dots, N_i^f\}$ are the volumic fractions of occupancy of each compartment and sum to one, D_{iso} is the diffusivity of free water and $\{\mathbf{D}_{j,i}, j = 1, \dots, N_i^f\}$ are tensors describing each compartment. The number of fascicles at each voxel N_i^f was estimated by assessing the generalization error of models of increasing complexities.³⁴ The DCI parameters at each voxel were estimated using the approach described in Scherrer *et al.*¹⁴

For comparison, we also estimated a single diffusion tensor at each voxel (DTI).³ Whole brain DTI and DCI tractography were performed using same parameters (seeding for all voxels with $\text{FA} > 0.25$; FA stopping criteria: $\text{FA} < 0.2$; angular stopping criteria: $\text{Angle} > 35^\circ$; 5 streamlines per voxel). We then selected streamlines going through a one-slice ROI drawn in the body of the corpus callosum.

3. RESULTS

Specimen container. Fig. 5 shows pictures of the two considered container strategies. In our experiments, we found that using the sealed bag provided 1) easier access to the brain; 2) easier visualization of residual air bubbles; and 3) easier removable of residual air bubble by massaging the specimen and applying a new seal. In addition, although the setup with the 3D printed brain holder used 64 coils, the SNR was lower due to the longer distance of each coil to the specimen. In the setup with the plastic bag we used 33 coils for acquisition but each coil was much closer to the tissue giving a higher SNR. We therefore chose to use the sealed bag container strategy.

Quantitative T2 mapping. The T2 measured in the white matter of the newborn specimen was 152ms,

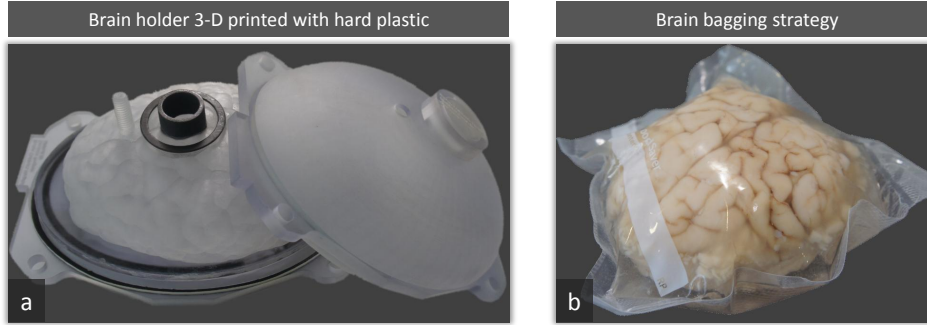


Figure 5. Illustration of the two container strategies. (a) 3-D printed brain holder. (b) brain in its sealed bag.

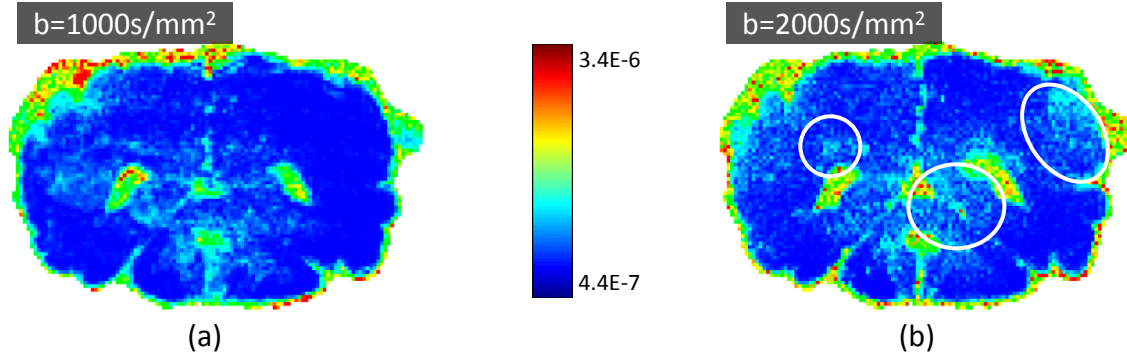


Figure 6. Amplitude of 95% confidence intervals on ADC estimates at each voxel. It shows that using $b = 1000\text{s/mm}^2$ provides narrower confidence intervals.

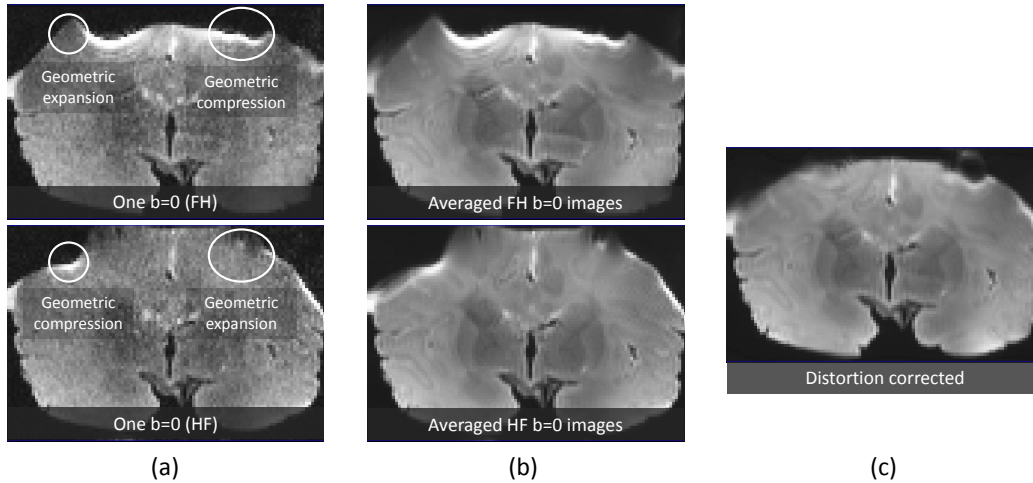


Figure 7. Distortion correction using acquisitions with opposite phase encoding direction. (a): One $b=0\text{s/mm}^2$ image acquired with phase encoding direction FH (top) and HF (bottom). (b): $b=0\text{s/mm}^2$ image averaged over the 17 repetitions for phase encoding direction FH (top) and HF (bottom), from which the susceptibility-induced off-resonance field is estimated. (c) $b=0\text{s/mm}^2$ image after distortion correction.

leading to a T2-relaxation induced attenuation factor of $\exp(-\frac{TE}{T_2}) = 0.53$ (for $TE=95\text{ms}$) which favorably compares to human adult *in-vivo* imaging (typically $T_2=80\text{ms}$ and $TE=95\text{ms}$ and therefore $\exp(-\frac{TE}{T_2}) = 0.31$)

Choice of optimal b-value range. The ADC measured in the WM of the fixed newborn specimen was $\approx 3.1\text{E}^{-4}\text{mm}^2/\text{s}$. It corresponds to an optimal b-value $b_{\text{optimal}} \approx 3600\text{s/mm}^2$ according to Jones *et al.*²⁹ We investigated the precision of ADC estimation when using a single-shell HARDI with $b = 1000\text{s/mm}^2$ and a

single-shell HARDI with $b = 2000\text{s/mm}^2$ with residual bootstrapping.³⁰ Fig. 6 reports the amplitude of 95% confidence intervals on ADC for the two acquisition strategies. It shows that the increased TE necessary to achieve $b = 2000\text{s/mm}^2$ compared to $b = 1000\text{s/mm}^2$ leads to larger confidence intervals and therefore to less reliable ADC estimates. We therefore used $b_{\text{inner}} = 1000\text{s/mm}^2$ for CUSP.

Correction of residual geometric and intensity distortion. Fig. 7 shows the geometric and intensity distortion caused by residual microscopic air bubbles. The distortion amplitude is especially large because high spatial resolution is achieved ($1 \times 1 \times 1\text{mm}^3$, matrix size = 128×76). Fig. 7c illustrates the corresponding corrected image.

High spatial resolution diffusion compartment imaging. Fig. 8 reports the results from high spatial resolution ($1 \times 1 \times 1\text{mm}^3$) diffusion compartment imaging. Fig. 8b shows that free water diffusion was detected in the ventricles, probably due to some remaining fixative solution that was unsuccessfully replaced by Galden in this region difficult to access inside the brain. Fig. 8c shows that the orientation of anisotropic DCI compartments matches the known anatomy and that crossing fascicles are detected, despite the known low diffusion anisotropy in newborn brains.³⁵ Finally, Fig. 9 reports the results from both DTI and DCI tractography. It shows that tract streamlines with DTI are prematurely stopped, likely due to the presence of crossings and due to the low diffusion anisotropy in newborn brains.³⁵ In contrast, DCI tractography provides streamlines with substantially larger extent that better matches the expected anatomy.

4. CONCLUSION

Post-mortem imaging enables long duration image acquisition that is conducive to higher resolution DW-MRI than is possible in vivo. However, imaging specimens for several hours requires fixation that alters tissue diffusivity.² This creates the need for appropriate choice of imaging solvent, distortion minimization and correction techniques, gradient encoding scheme, optimal b-values and acquisition matrix size in order to obtain high quality multi b-value DW images.

In this work we considered the specific requirements of post-mortem imaging together with the constraints of clinical scanners to design an optimal protocol for *ex-vivo* diffusion compartment imaging. Our protocol enables post-mortem DCI investigations of neuropathologies and of the brain connectivity using conventional clinical scanners which are available to a large number of researchers and, unlike most animal scanners, have a bore diameter large enough to image a whole human brain.

In future work we will evaluate the benefits of using read-out segmented EPI (ros-EPI)³⁶ instead of conventional EPI to reduce geometric and intensity distortion. The scan duration time when using ros-EPI is directly proportional to the number of segments used, limiting the number of repetitions achievable for a fixed scan time. We will evaluate the impact on SNR, distortion and ultimately on confidence intervals on DCI parameters of using ros-EPI instead of conventional EPI.

Acknowledgment

This work was supported in part by NIH grants 1U01NS082320, R01 NS079788-01A1, R01 EB008015, R01 EB013248, P30 HD018655, R42 MH086984 and UL1 TR000170.

Appendix: CUSP90 Gradient Encoding Scheme.

We provide the CUSP90 gradient set in the Siemens format. Gradients with high b-value were distributed throughout the table to reduce the scanner burden. Imaging CUSP90 with an inner-shell with b-value b_{inner} requires to set the imaged b-value to $3b_{\text{inner}}$ in the Siemens diffusion tab (Free Mode). This is because the b-value provided in Free Mode corresponds to the b-value of the gradient with largest norm ($\pm 1, \pm 1, \pm 1$). With this choice, the resulting minimum achievable TE correctly matches the minimum achievable TE of a single-shell HARDI at b_{inner} .

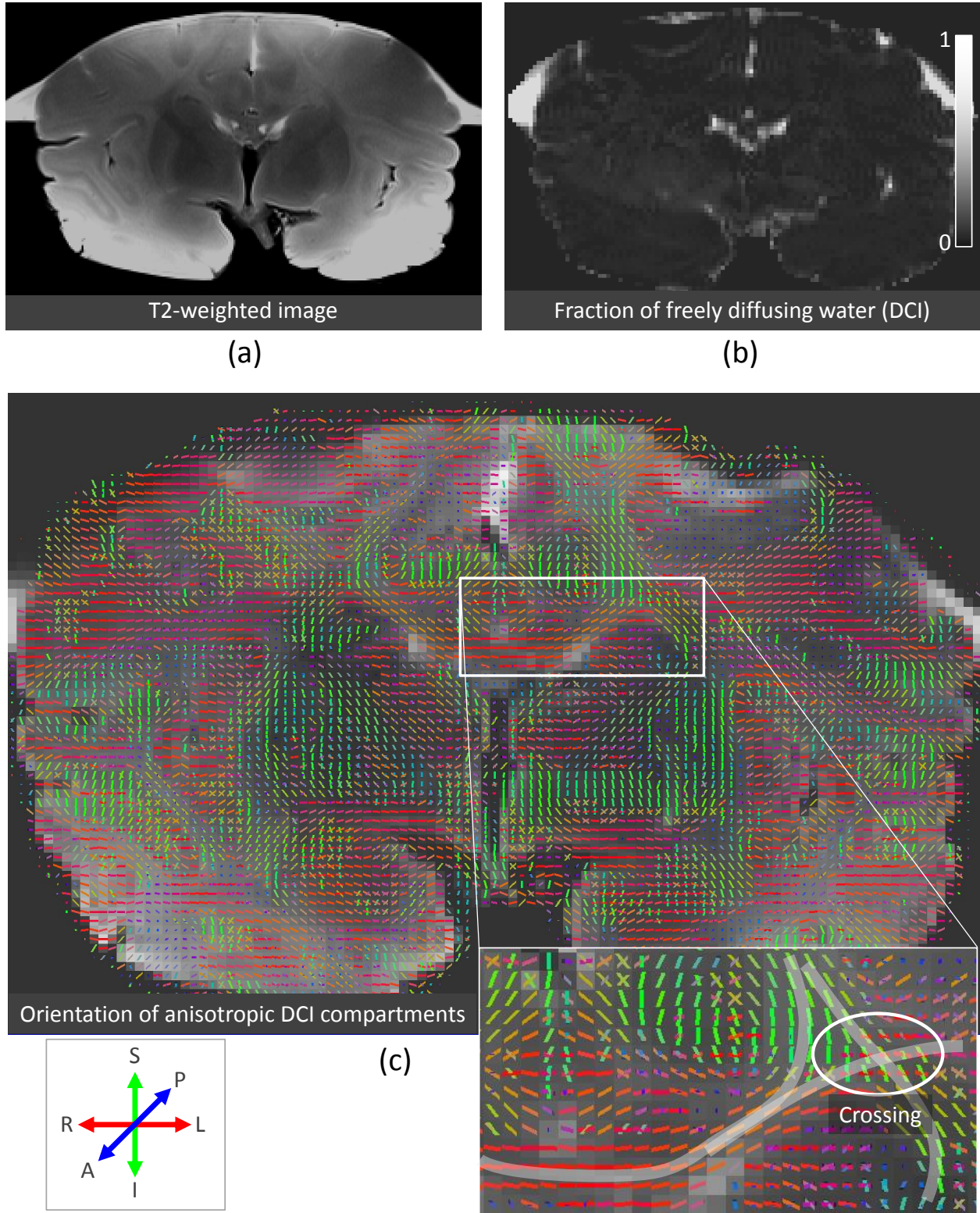


Figure 8. (a) T2-weighted image. (b) Fraction of freely diffusing water at each voxel. (c) Orientation of each anisotropic compartment superimposed on the $b = 0$ s/mm² image. A region in which crossing fascicles are estimated is highlighted.

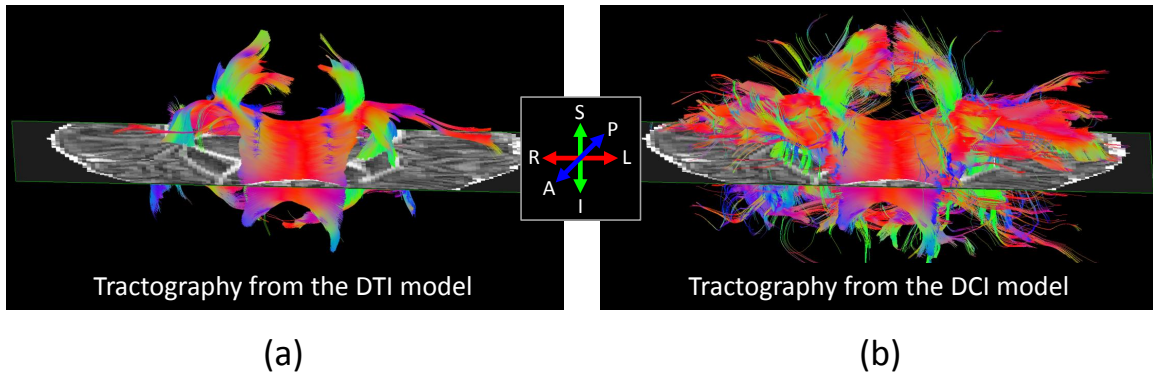


Figure 9. Tractography results for both DTI (a) and DCI (b).

```

[directions=90]
CoordinateSystem = xyz
Normalisation = none
Vector[0] = ( 0.00000, 0.00000, 0.00000 )
Vector[1] = ( 0.00000, 0.00000, 0.00000 )
Vector[2] = ( -1.00000, -1.00000, -1.00000 )
Vector[3] = ( 1.00000, 0.00000, 0.00000 )
Vector[4] = ( 0.16600, 0.98600, 0.00000 )
Vector[5] = ( 0.11000, -0.66400, -0.74000 )
Vector[6] = ( 0.90100, -0.41900, -0.11000 )
Vector[7] = ( 0.16900, 0.60100, -0.78100 )
Vector[8] = ( 0.81500, 0.38600, -0.43300 )
Vector[9] = ( -0.65600, -0.36600, -0.66000 )
Vector[10] = ( 0.00000, 0.00000, 0.00000 )
Vector[11] = ( 1.00000, -1.00000, -1.00000 )
Vector[12] = ( -0.58200, -0.80000, -0.14300 )
Vector[13] = ( -0.90000, -0.25900, -0.35000 )
Vector[14] = ( -0.69300, 0.69800, -0.17800 )
Vector[15] = ( 0.35700, -0.92400, -0.14000 )
Vector[16] = ( 0.54300, -0.48800, -0.68300 )
Vector[17] = ( 0.52500, 0.39600, -0.75300 )
Vector[18] = ( 0.63900, -0.68900, -0.34100 )
Vector[19] = ( 0.00000, 0.00000, 0.00000 )
Vector[20] = ( -1.00000, 1.00000, -1.00000 )
Vector[21] = ( -0.33000, -0.01300, -0.94400 )
Vector[22] = ( 0.52400, 0.78300, -0.33500 )
Vector[23] = ( 0.60900, -0.06500, -0.79100 )
Vector[24] = ( 0.22000, -0.23300, -0.94700 )
Vector[25] = ( -0.00400, -0.91000, -0.41500 )
Vector[26] = ( -0.51100, 0.62700, -0.58900 )
Vector[27] = ( -0.41400, -0.73700, -0.53500 )
Vector[28] = ( 0.00000, 0.00000, 0.00000 )
Vector[29] = ( 1.00000, 1.00000, -1.00000 )
Vector[30] = ( -0.67900, 0.13900, -0.72100 )
Vector[31] = ( -0.88400, 0.29600, -0.36200 )
Vector[32] = ( -0.26200, -0.43200, -0.86300 )
Vector[33] = ( 0.08800, 0.18500, -0.97900 )
Vector[34] = ( -0.29400, 0.90700, -0.30200 )
Vector[35] = ( 0.88700, -0.08900, -0.45300 )
Vector[36] = ( -0.25700, 0.44300, -0.85900 )
Vector[37] = ( 0.00000, 0.00000, 0.00000 )
Vector[38] = ( 1.00000, 1.00000, 0.00000 )
Vector[39] = ( 0.08600, 0.86700, -0.49100 )
Vector[40] = ( 0.86300, 0.50400, -0.02500 )
Vector[41] = ( 1.00000, -0.18020, -0.20590 )
Vector[42] = ( 0.46220, 1.00000, -0.75080 )
Vector[43] = ( -0.04830, -0.09000, -1.00000 )
Vector[44] = ( 1.00000, 0.21090, -0.32670 )
Vector[45] = ( -0.55680, -0.28080, -1.00000 )
Vector[46] = ( 0.00000, 0.00000, 0.00000 )
Vector[47] = ( 0.00000, -1.00000, -1.00000 )
Vector[48] = ( -1.00000, -0.27520, -0.05050 )
Vector[49] = ( 0.42240, 0.13530, -1.00000 )
Vector[50] = ( -0.56590, 0.35890, -1.00000 )
Vector[51] = ( -0.33420, -1.00000, -0.34050 )
Vector[52] = ( 0.42990, 1.00000, -0.15040 )
Vector[53] = ( -1.00000, 0.51240, -0.20340 )
Vector[54] = ( 0.09110, -1.00000, -0.13310 )
Vector[55] = ( 0.00000, 0.00000, 0.00000 )
Vector[56] = ( -1.00000, 0.00000, -1.00000 )
Vector[57] = ( -1.00000, 0.02390, -0.43890 )
Vector[58] = ( 0.39690, -1.00000, -0.58550 )
Vector[59] = ( -0.52710, 1.00000, -0.14230 )
Vector[60] = ( 0.01210, 0.44840, -1.00000 )
Vector[61] = ( -1.00000, -0.71170, -0.42350 )
Vector[62] = ( 0.05690, -0.46620, -1.00000 )
Vector[63] = ( 1.00000, -0.46500, -0.59580 )
Vector[64] = ( 0.00000, 0.00000, 0.00000 )
Vector[65] = ( -1.00000, 1.00000, 0.00000 )
Vector[66] = ( -0.02240, 1.00000, -0.25290 )
Vector[67] = ( 0.86020, -0.24200, 0.03790 )
Vector[68] = ( 0.48110, 0.33730, 0.67440 )
Vector[69] = ( -0.42240, 0.09940, 0.78210 )
Vector[70] = ( -0.19110, 0.83790, 0.24770 )
Vector[71] = ( 0.22740, -0.56800, 0.65240 )
Vector[72] = ( -0.60160, -0.62690, 0.21230 )
Vector[73] = ( 0.00000, 0.00000, 0.00000 )
Vector[74] = ( 0.00000, 1.00000, -1.00000 )
Vector[75] = ( -0.34100, -0.24170, 0.65210 )
Vector[76] = ( 0.70050, 0.32220, 0.07430 )
Vector[77] = ( 0.46390, -0.30070, 0.54260 )
Vector[78] = ( 0.11770, 0.43100, 0.63280 )

```

Vector[79] = (-0.60190, 0.41770, 0.25150)	Vector[85] = (-0.43810, 0.21880, 0.40020)
Vector[80] = (-0.04180, -0.76620, 0.10560)	Vector[86] = (0.29580, -0.53310, 0.16830)
Vector[81] = (0.14950, 0.52120, 0.32560)	Vector[87] = (-0.34770, -0.43280, 0.30300)
Vector[82] = (0.00000, 0.00000, 0.00000)	Vector[88] = (0.11740, -0.07570, 0.61680)
Vector[83] = (1.00000, 0.00000, -1.00000)	Vector[89] = (0.00000, 0.00000, 0.00000)
Vector[84] = (0.60300, 0.05650, 0.18220)	

REFERENCES

- [1] Lerch, J. P., Gazdzinski, L., Germann, J., Sled, J. G., Henkelman, R. M., and Nieman, B. J., “Wanted dead or alive? the tradeoff between in-vivo versus ex-vivo MR brain imaging in the mouse,” *Front. Neuroinform.* **6** (2012).
- [2] Sun, S.-W., Neil, J. J., Liang, H.-F., He, Y. Y., Schmidt, R. E., Hsu, C. Y., and Song, S.-K., “Formalin fixation alters water diffusion coefficient magnitude but not anisotropy in infarcted brain,” *Magn Reson Med* **53**(6), 1447–1451 (2005).
- [3] Basser, P. J., Mattiello, J., and LeBihan, D., “Estimation of the effective self-diffusion tensor from the NMR spin echo,” *J Magn Reson B* **103**(3), 247–254 (1994).
- [4] Kinnunen, K., Greenwood, R., Powell, J., Leech, R., Hawkins, P., Bonnelle, V., Patel, M., Counsell, S., and Sharp, D., “White matter damage and cognitive impairment after traumatic brain injury,” *Brain* **134**, 449–463 (2011).
- [5] Voineskos, A. N., Lobaugh, N. J., Bouix, S., Rajji, T. K., Miranda, D., Kennedy, J. L., Mulsant, B. H., Pollock, B. G., and Shenton, M. E., “Diffusion tensor tractography findings in schizophrenia across the adult lifespan,” *Brain* **133**(Pt 5), 1494–1504 (2010).
- [6] Sajjadi, S. A., Acosta-Cabrero, J., Patterson, K., Diaz-de Grenu, L. Z., Williams, G. B., and Nestor, P. J., “Diffusion tensor magnetic resonance imaging for single subject diagnosis in neurodegenerative diseases,” *Brain* **136**(Pt 7), 2253–2261 (2013).
- [7] Metzler-Baddeley, C., O’Sullivan, M. J., Bells, S., Pasternak, O., and Jones, D. K., “How and how not to correct for CSF-contamination in diffusion MRI,” *NeuroImage* **59**(2), 1394–1403 (2012).
- [8] Syková, E. and Nicholson, C., “Diffusion in brain extracellular space,” *Phys Rev* **88**(4), 1277–340 (2008).
- [9] Vos, S. B., Jones, D. K., Jeurissen, B., Viergever, M. A., and Leemans, A., “The influence of complex white matter architecture on the mean diffusivity in diffusion tensor MRI of the human brain,” *NeuroImage* **59**(3), 2208–2216 (2012).
- [10] Jones, D. K., Knösche, T. R., and Turner, R., “White matter integrity, fiber count, and other fallacies: the do’s and don’ts of diffusion MRI,” *NeuroImage* **73**, 239–254 (2013).
- [11] Tournier, J. D., Calamante, F., Gadian, D. G., and Connelly, A., “Direct estimation of the fiber orientation density function from diffusion-weighted MRI data using spherical deconvolution,” *NeuroImage* **23**(3), 1176–1185 (2004).
- [12] Tuch, D. S., “Q-ball imaging,” *Magn Reson Med* **52**(6), 1358–1372 (2004).
- [13] Latour, L., Svoboda, K., Mitra, P., and Sotak, C., “Time-dependent diffusion of water in a biological model system,” *Proc Natl Acad Sci U S A* **91**(4), 1229–1233 (1994).
- [14] Scherrer, B. and Warfield, S. K., “Parametric Representation of Multiple White Matter Fascicles from Cube and Sphere Diffusion MRI,” *PLoS ONE* **7**(11) (2012).
- [15] Stanisz, G. J., Szafer, a., Wright, G. a., and Henkelman, R. M., “An analytical model of restricted diffusion in bovine optic nerve,” *Magn Reson Med* **37**(1), 103–111 (1997).
- [16] Norris, D. G., “The effects of microscopic tissue parameters on the diffusion weighted magnetic resonance imaging experiment,” *NMR Biomed* **14**(2), 77–93 (2001).
- [17] Taquet, M., Scherrer, B., Commowick, O., Peters, J. M., Sahin, M., Macq, B., and Warfield, S. K., “A Mathematical Framework for the Registration and Analysis of Multi-Fascicle Models for Population Studies of the Brain Microstructure,” *IEEE Trans Med Imaging* **2**(33), 504–17 (2014).
- [18] Scherrer, B. and Warfield, S. K., “Why multiple b-values are required for multi-tensor models. Evaluation with a constrained log-Euclidean model,” in *[ISBI]*, 1389–1392 (2010).
- [19] Assaf, Y., Freidlin, R. Z., Rohde, G. K., and Basser, P. J., “New modeling and experimental framework to characterize hindered and restricted water diffusion in brain white matter,” *Magn Reson Med* **52**(5), 965–78 (2004).
- [20] Kroenke, C. D., Bretthorst, G. L., Inder, T. E., and Neil, J. J., “Diffusion MR imaging characteristics of the developing primate brain,” *NeuroImage* **25**(4), 1205–1213 (2005).
- [21] Miller, K. L., Stagg, C. J., Douaud, G., Jbabdi, S., Smith, S. M., Behrens, T. E. J., Jenkinson, M., Chance, S. A., Esiri, M. M., Voets, N. L., Jenkinson, N., Aziz, T. Z., Turner, M. R., Johansen-Berg, H., and McNab, J. A., “Diffusion imaging of whole, post-mortem human brains on a clinical MRI scanner,” *NeuroImage* **57**(1), 167–181 (2011).
- [22] Jezzard, P. and Clare, S., “Sources of distortion in functional MRI data,” *Hum Brain Mapp* **8**(2-3), 80–85 (1999).
- [23] Jezzard, P. and Balaban, R. S., “Correction for geometric distortion in echo planar images from B0 field variations,” *Magn Reson Med* **34**(1), 65–73 (1995).

- [24] Wansapura, J. P., Holland, S. K., Dunn, R. S., and Ball, W. S., "NMR relaxation times in the human brain at 3.0 tesla," *J Magn Reson Imaging* **9**(4), 531–538 (1999).
- [25] Counsell, S. J., Kennea, N. L., Herlihy, A. H., Allsop, J. M., Harrison, M. C., Cowan, F. M., Hajnal, J. V., Edwards, B., Edwards, A. D., and Rutherford, M. A., "T2 relaxation values in the developing preterm brain.," *Am J Neuroradiol* **24**(8), 1654–1660 (2003).
- [26] Dawe, R. J., Bennett, D. A., Schneider, J. A., Vasireddi, S. K., and Arfanakis, K., "Postmortem MRI of human brain hemispheres: T2 relaxation times during formaldehyde fixation.," *Magn Reson Med* **61**(4), 810–818 (2009).
- [27] Le Bihan, D., "Molecular diffusion nuclear magnetic resonance imaging," *Magn Reson Q* **7**(1), 1–30 (1991).
- [28] Cook, P. A., Symms, M., Boulby, P. A., and Alexander, D. C., "Optimal acquisition orders of diffusion-weighted MRI measurements," *J Magn Reson Imaging* **25**(5), 1051–1058 (2007).
- [29] Jones, D. K., Horsfield, M. A., and Simmons, A., "Optimal strategies for measuring diffusion in anisotropic systems by magnetic resonance imaging.," *Magn Reson Med* **42**(3), 515–525 (1999).
- [30] Chung, S., Lu, Y., and Henry, R. G., "Comparison of bootstrap approaches for estimation of uncertainties of DTI parameters," *Neuroimage* **33**(2), 531–541 (2006).
- [31] Whitcher, B., Tuch, D. S., Wisco, J. J., Sorensen, A. G., and Wang, L., "Using the wild bootstrap to quantify uncertainty in diffusion tensor imaging," *Hum Brain Mapp* **29**(3), 346–362 (2008).
- [32] Andersson, J. L. R., Skare, S., and Ashburner, J., "How to correct susceptibility distortions in spin-echo echo-planar images: application to diffusion tensor imaging.," *NeuroImage* **20**(2), 870–888 (2003).
- [33] Tuch, D. S., Reese, T. G., Wiegell, M. R., Makris, N., Belliveau, J. W., and Wedeen, V. J., "High angular resolution diffusion imaging reveals intravoxel white matter fiber heterogeneity," *MRM* **48**(4), 577–582 (2002).
- [34] Scherrer, B., Taquet, M., and Warfield, S. K., "Reliable Selection of the Number of Fascicles in Diffusion Images by Estimation of the Generalization Error," in *[IPMI], LNCS 7917*, 742–753 (2013).
- [35] Sakuma, H., Nomura, Y., Takeda, K., Tagami, T., Nakagawa, T., Tamagawa, Y., Ishii, Y., and Tsukamoto, T., "Adult and neonatal human brain: diffusional anisotropy and myelination with diffusion-weighted MR imaging.," *Radiology* **180**(1), 229–233 (1991).
- [36] Holdsworth, S. J., Skare, S., Newbould, R. D., Guzmán, R., Blevins, N. H., and Bammer, R., "Readout-segmented EPI for rapid high resolution diffusion imaging at 3 T.," *Eur J Radiol* **65**(1), 36–46 (2008).